



Cite this: *Mater. Adv.*, 2022,  
3, 8108Received 24th June 2022,  
Accepted 3rd October 2022

DOI: 10.1039/d2ma00736c

rsc.li/materials-advances

# Synthesis, aromaticity, charge transport in OFET devices and nonlinear optical properties of tetrathia/oxa[22]porphyrin(2.1.2.1)s: a decade of progress

Kamaljit Singh \* and Paramjit Kaur 

Distinctive physicochemical characteristics, aromaticity–antiaromaticity relations, electrochemistry, charge transport in organic-field effect transistor devices (thin films and single crystals), supramolecular donor–acceptor dyads, photoresponsivity, and linear and nonlinear optical behaviour (2nd and 3rd-order) of rather under-appreciated classes of meso-substituted tetrathia/oxa[22]porphyrin(2.1.2.1)s explored by our group await further exploration to open new possibilities in organic electronics. This personal account discusses the above attributes including the structure dependent p-channel and ambipolar charge transport in tetrathia/oxa[22]porphyrin(2.1.2.1)s and their donor–acceptor dyads with tetracyanoethylene and C<sub>60</sub>/C<sub>70</sub> fullerenes, respectively. Also we discuss the reverse saturation absorption, two-photon absorption and third-order nonlinear polarizability of tetrathia[22]porphyrin(2.1.2.1)s.

## 1. Introduction

Porphyrinoids have attained undisputed status in supramolecular chemistry, biology and materials science owing to their outstanding structural diversity and properties attributed to their inbuilt physicochemical features, well-defined structures

and  $\pi$ -conjugation.<sup>1</sup> Such compounds display interesting biological, optical, photophysical, electronic and magnetic properties and find applications in the areas of non-linear optics,<sup>2a,b</sup> two-photon absorption materials,<sup>1a</sup> organic light emitting diodes,<sup>2c</sup> dye sensitized solar cells,<sup>2d</sup> organic semiconductors,<sup>2e</sup> and artificial photosynthesis,<sup>2f</sup> as materials for imaging and photodynamic therapy,<sup>2g</sup> etc. Aromaticity of such porphyrinoids in terms of cyclic delocalization of the mobile electrons is a distinctive feature, which allows switching to antiaromatic

Department of Chemistry, Centre of Advanced Study, Guru Nanak Dev University, Amritsar – 143 005, India. E-mail: kamaljit.chem@gndu.ac.in



Professor Kamaljit Singh (Right) Professor Paramjit Kaur(Left)

Professor Kamaljit Singh (Right) received PhD degree from Guru Nanak Dev University (GNDU) in 1989. He was postdoctoral fellow at National Institute of Organic Chemistry (CSIC), Madrid, working on carbohydrate chemistry. He has varied research interests spanning from synthetic organic/medicinal chemistry to material chemistry and is author of over 160 research papers, several reviews and book chapters. He has been an INSA-RSC and The British Council visiting fellow at UMIST, UK and Brainpool visiting fellow at Kangwon National University, South Korea. He was awarded Bronze Medal by Chemical Research Society of India (2009). He is also a recipient of Professor K. Venkataraman endowment lecture award (2015). Professor Paramjit Kaur (Left) received her PhD degree from Guru Nanak Dev University in 1990. She did a post-doctorate at the Departamento de Química Inorganica at Universidad

Complutense de Madrid before joining as a Lecturer in the Department of Chemistry at Guru Nanak Dev University in 1997, where she is now a full Professor. She is author of over 80 research papers, review articles and book chapters. Her research interest focuses on analyte detection using fluorescence probes and nonlinear optical materials.



structures upon suitable alteration of the macrocyclic conjugation pathway. Synthesis of porphyrinoids through modification of the macrocyclic core, and/or the size and topology of the macrocyclic framework, and substitution pattern has led to the understanding of the structure–property relationship of these important classes of macrocycles.<sup>3</sup> Altering the macrocyclic core by replacing one or more pyrrole rings with other heterocyclic or carbocyclic rings constitutes a promising approach to tune the aromaticity, binding ability, and electronic and photochemical properties of porphyrins. Consequently, understanding of the effect of structure modification on aromaticity–antiaromaticity (Huckel and Mobius)<sup>4</sup> relationships, and photophysical and functional properties of new classes of porphyrins is of tremendous significance.

Among a variety of structurally diverse classes of porphyrins, tetrathia[22]porphyrin(2.1.2.1)s (TTPs hereinafter) and their oxygen analogues, tetraoxa[22]porphyrin(2.1.2.1)s (TOPs hereinafter) have presented themselves as efficient materials owing to flexibility in synthesis and interesting structural features compared to the tetrapyrrolic counterparts. The aromaticity of these systems is not lost even upon ring puckering under the influence of substituents at the *meso*-positions. Owing to the favourable energies of the frontier molecular orbitals, these porphyrinoids exhibit efficient p-channel charge transport in thin film and/or single crystal based organic field-effect transistor (OFET) devices. Further, being efficient donors, TTPs in combination with strong acceptors produce stable charge transfer type complexes. Overall, these porphyrinoids are purported to be candidates for the next generation organic electronics owing to tailorability of the structure dependent functional properties.

Porphyrins are also endowed with large optical nonlinearities, fast response time, broad-band spectral response and other superior optoelectronic attributes. However, finding new porphyrinoids capable of strong nonlinear optical behaviour for applications in fluorescence microscopy, photodynamic therapy, two-photon excitation, 3D microfabrication, sensor protection, optical data storage and optical limiting has been a very sought after objective. Particularly, there have been

intense efforts for improvement of the nonlinear optical properties such as molecular second hyperpolarizability,  $\gamma$ , excited state absorption cross-section,  $\sigma$ , *etc.* For this purpose, due to extended  $\pi$ -electron conjugation, TTPs/TOPs were expected to show large excited state absorption cross-sections leading to reverse saturation absorption (RSA), high nonlinear refractive index coefficient and nonlinear absorption coefficient values and fast response times.

In this personal account, we intend to discuss various aspects related to the design, synthesis, structure, linear optical properties, aromaticity/antiaromaticity, and redox behaviour of TTPs/TOPs. In addition, we also explore the semiconducting and nonlinear optical (NLO) behaviour of these scantily studied porphyrinoids. For the sake of brevity and objectivity, this account excludes general discussion of the porphyrin chemistry, detailed synthesis and properties of all other classes of porphyrins, for which excellent review articles have already been published.<sup>1,5</sup>

## 2. Meso-substituted TTPs/TOPs: charge transport in thin film and single crystal organic field-effect transistor devices

### 2.1. Synthesis

The first synthesis of the neutral aromatic TTP 5 [also named sulphur bridged[22]annulene(2.1.2.1) in the annulene nomenclature] was reported by Cava<sup>6</sup> and is outlined in Scheme 1. The intermediate 5,16-dihydro TTP 4 (Scheme 1) was obtained through a McMurry coupling reaction of 5,5'-methylenebis(thiophene-2-carbaldehyde) 3 using titanium tetrachloride/zinc. Compound 3 in turn was obtained from 2-bromothiophene *via* intermediate 2. Compound 4 was dehydrogenated<sup>6</sup> by 2,3-dichloro-5,6-dicyano-1,4-benzoquinone (DDQ)/hydrazine to furnish 5. The aromaticity of 5 was evidenced by its <sup>1</sup>H NMR and UV-visible absorption spectra.

The appearance of two singlets at  $\delta$  11.36 and 12.34 ppm corresponding to ethene carbons and an AB splitting pattern of the thiophene protons ( $\delta$  10.84 and 10.86 ppm) in the <sup>1</sup>H NMR



Scheme 1 Synthesis of aromatic tetrathia[22]porphyrin(2.1.2.1) 5.



spectrum of **5** suggested the presence of strong aromatic ring currents. The considerably redshifted UV-visible absorption spectrum showed sharp Soret and Q type bands at 417, 503, 540, 579, and 771 nm. This contrasted the broad peaks observed in the absorption spectra of the antiaromatic counterparts.<sup>7</sup> Further, **5** is comparatively less crowded, enabling it to have a planar or near-planar structure with the conjugated  $\pi$ -electrons around the periphery.

In the solid state, the molecules of **5** packed into a sandwich-herringbone arrangement. Further, good thermal stability was observed by thermogravimetric analysis.

The revelation of the structural features of **5** stimulated us to design a more practicable, general synthetic route to procure structurally decorated **5** (and its oxygen analogues) and to investigate their structure, optical properties, and electrochemical behaviour in order to develop potential applications as organic semiconductors and NLO materials. We also planned to investigate the charge transport behaviour of these porphyrinoids in organic field-effect transistor (OFET) devices. The reason for this was the fact that OFETs attracted considerable interest due to their potential applications in low-cost, large area and flexible electronics, such as radiofrequency identification (RFID) tags, flexible displays, *etc.*<sup>8</sup> Since the performance of OFETs is influenced by such factors as the molecular structure, solid-state packing, film morphology and material stability, we investigated the molecular structure and its relationship with aromaticity, the influence of geometry of the macrocyclic core on these properties, effect of substituents at the methine carbons (*meso*-positions) of **5** as well as their corresponding oxygen bridged analogues (*vide infra*). In this context, the flexibility of appending electron-withdrawing or electron-donating groups at the *meso*-positions was recognized to be an attractive attribute as it modulated the charge transport properties, especially the field-effect mobility and/or current on/off ratios, of the OFET devices fabricated from these compounds. These properties have been discussed in a later section.

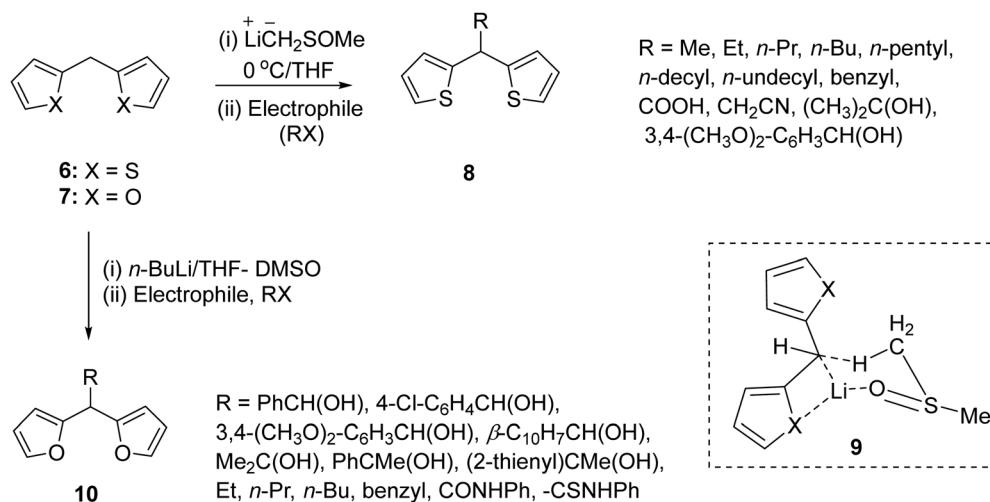
In order to develop a general route to the synthesis of TTPs/TOPs, we envisaged the synthesis of *meso*-substituted

bis(heterocyclyl)methanes so that the key bis-formyl-di(thien/furan-2-yl)methane precursor is prefunctionalized at the *meso*-position without resorting to the synthesis of a number of *meso*-elaborated **2** (Scheme 1).

The most general route to the synthesis of di(thien/furan-2-yl)methane would involve acid catalysed condensation of thiophene/furan with a carbonyl compound. However, this route faces limitations in the case of aliphatic aldehydes owing to the limitation of showing side reactions such as polymerization, aldol condensation, and oxidation to carboxylic acids. Additionally the non-availability of many functionalized aldehydes would preclude the synthesis of di(thien/furan-2-yl)methane derivatives substituted with a functionalized chain at the *meso*-position. To avoid these limitations and realize our objective, we sought to employ a lithiation–substitution protocol<sup>9–11</sup> (Scheme 2). This new route furnished access to a number of *meso*-substituted di(thien-2-yl)methanes **8** and di(furan-2-yl)methanes **10** in a synthetically useful manner.

This approach allowed incorporation of those groups at the *meso*-positions of **8** and **10**, which are otherwise difficult to append through an aldehyde condensation approach. The regioselectivity of the deprotonation (Scheme 2) of **6** and **7** was proposed *via* transition state **9** and the higher acidity of the protons at the *meso*- ( $pK_a < 30.2$ ) than the C-5 ( $pK_a = 35$ ) position.

Having successfully obtained the putative intermediates **8** and **10**, diformylation expeditiously furnished (Scheme 3) the corresponding bis-formyl-(dithien-2-yl)methane **11** or bis-formyl-(difuran-2-yl)methane **12** derivatives. Starting from **11**, the synthesis of *meso*-functionalized 5,16-dihydro TTPs **13** ( $R = \text{Me, Et, } n\text{-Pr, } n\text{-Bu, } n\text{-pentyl, } n\text{-decyl, } n\text{-undecyl, benzyl, COOH, or CH}_2\text{CN}$ ) was achieved by using standard McMurry coupling reaction conditions. Thus, overall starting from **8**, the synthesis of **13** bearing a variety of long aliphatic chains at the 5,16-positions (*meso*-positions) constituted a useful synthetic sequence. However, we realized that the McMurry coupling reaction was extremely sensitive to moisture and demanded starting materials of very high purity. Notwithstanding these precautions, the yield



Scheme 2 Highly regioselective synthesis of di-(thien-2-yl)methanes and di-(furan-2-yl)methanes employing a lithiation–substitution protocol.





Scheme 3 A generalized synthesis of *meso*-substituted 5,16-dihydro TTPs/TOPs **13/14**.

of **13/14** was invariably low. Thus, using this synthetic strategy, while the limitations of the aldehydes were obviated, obtaining differently *meso*-substituted **13/14**, following this route was cumbersome. Further, the need to run all the preceding synthetic steps including diformylation of appropriate **8/10** as well as McMurry coupling reactions for each compound rendered the strategy less efficient.

As an alternative approach, we developed a metalation protocol for regioselective generation of carbanion at the *meso*-position of 5,16-dihydro TTP **4** (Scheme 4)<sup>12</sup> and obtained the dianionic analogue **15**. Subsequent reaction with an appropriate electrophile paved the way for a number of *meso*-substituted 5,16-dihydro TTPs **13**. This protocol avoided repetitive bis-formylation reactions of **8** as well as the need to perform low-yielding McMurry coupling reaction for each **11**.

However, our attempts to oxidize the nonaromatic *meso*-elaborated **13** (Scheme 4) with DDQ/hydrazine and a number of other reagents met with failure. This is due to the sp<sup>3</sup> hybridization at the 5- and 16-positions of **13**, and the consequent ring puckering. Presumably, the more flexible alkyl substituents at the *meso*-positions could not enforce planarity to rein in aromaticity in the macrocycle upon oxidation.

Appending aromatic substituents on the *meso*-positions of **13** or **14** appeared particularly attractive as it would have

furnished derivatives required to understand the influence of *meso*-substituents on aromaticity. Also it would have allowed access to the hitherto elusive *meso*-aryl substituted analogues of **22** and **23** upon oxidation of the intermediate 5,16-dihydro analogues. In this context, the synthesis of *meso*-aryl substituted building blocks **16** and **17** was conveniently achieved through the known aldehyde-thiophene/furan condensation routes as described above. Facile transformation of **16** (and **17**) to the corresponding diformyl derivatives **18** (and **19**) was achieved by employing a lithiation-formylation sequence of reactions in the former and Vilsmeier Haack reaction conditions in the latter (Scheme 5).<sup>13,14</sup> McMurry type coupling of these intermediates using low valent titanium furnished the 5,16-diaryldihydro- TTP **20** or TOP **21** in good yields. Subsequent two-electron oxidation using DDQ/hydrazine resulted in smooth transformation to the corresponding 5,16-diaryl TTPs **22** and TOPs **23** in a synthetically useful manner. As is evident from Scheme 5, a number of *meso*-aryl substituents with varying steric bulk could be incorporated in **22** and **23**.

## 2.2. Structure, aromaticity and redox behaviour

As a representative example,<sup>13</sup> in the <sup>1</sup>H NMR spectrum of **22a**, the methine carbons appeared as a singlet at δ 11.08 ppm. Additionally, the thiophene protons appeared at δ 10.38 and 10.01 ppm as an AB quartet. The coupling constant (*J*<sub>vic</sub> = 4.5–5.0 Hz) of the thiophene



Scheme 4 Regioselective lithiation-substitution protocol for the direct synthesis of 5,16-dihydro TTPs.





Scheme 5 Synthesis of neutral, aromatic 5,16-diaryl TTPs/TOPs.

protons in **22a** was partially equalized, indicating delocalization of electrons. The protons of the *meso*-aryl group appeared at  $\delta$  8.46 and 8.00 ppm. Overall the chemical shifts of the protons of **22a** were significantly downfield in analogy to aromatic porphyrinoids. Further, unlike the 5,16-dihydro derivative **20a**, none of the protons of **22a** appeared upfield to  $\delta$  7.39 ppm.

On the other hand, the <sup>1</sup>H NMR spectrum of oxygen analogue **23a**<sup>14</sup> was very characteristic as it differed from that of its sulphur analogue **22a**. As expected, in the <sup>1</sup>H NMR spectrum of 5,16-dihydro TOP **21a**, the furan  $\beta$ -protons appeared as a pair of doublets and the singlet for the signal of methine protons was relatively upfield. The magnitude of the vicinal coupling constants was very similar to pristine furan, indicating the thermodynamically more stable double-bond character of the furan units. In contrast, in the <sup>1</sup>H NMR spectrum of the  $(4n+2)\pi$  analogue **23a**, not only did the AB system of the furan appear significantly downfield compared to **21a**, the coupling constant was also partially equalized indicating delocalization and none of the proton signals of the porphyrin framework appeared upfield to  $\delta$  9.01 ppm. Interestingly, as a characteristic feature of **23a**, one of the methine proton pairs resonated significantly upfield to appear at  $\delta$  -5.42 ppm, indicating the influence of aromatic ring currents and difference in the topology of the macrocyclic framework.

As a quantitative probe of aromaticity, Nucleus-Independent Chemical Shift, NICS(1), analysis using *ab initio* quantum mechanical density functional theory (DFT) calculations at the B3LYP/6-31G(d) level, using the Gauge Independent Atomic Orbital (GIAO) method, revealed large negative NICS values. As a representative case, NICS(1)<sup>15</sup> values for **23a** ( $\delta$  -13.17) and **22d** ( $\delta$  -13.30; ppm) are shown in Fig. 1. The values at the

centre of the macrocyclic ring as well as individual heterocyclic and *meso* aromatic rings indicated a greater degree of aromaticity owing to the enhanced ring current effects of a planar geometry. The shapes of the plots of the chemical shifts *vs.* distance of the NICS probe, a ghost atom (termed “bq” after the ghost Banquo in Shakespeare’s *Macbeth*) from the molecular plane furnished a proof of diamagnetic ring currents.

The FAB mass spectra of **22a** and **23a** and other members of the series indicated the exceptional stability of these porphyrinoids as these showed only a strong molecular ion peak (100%) without fragmentation. The good thermal stability of **22a**, **23a** and other analogues was also indicated by the onset thermal decomposition temperature in the thermogravimetric analyses, which was more than 370 °C. Further, these porphyrinoids showed air stability and did not require an inert atmosphere for handling/storage.

The characteristic feature of the UV-visible absorption spectrum of **22a** (Fig. 2) was the presence of a sharp and strong absorption band at 429 nm ( $\epsilon_{\text{max}} = 222\,860 \text{ dm}^3 \text{ mol}^{-1} \text{ cm}^{-1}$ ), which was absent in the corresponding dihydro derivative **20a**. In addition, several weaker absorptions at longer wavelengths [519, 557, 600 and 777 nm ( $\epsilon_{\text{max}} = 2900, 9200, 57\,380$  and  $1700 \text{ dm}^3 \text{ mol}^{-1} \text{ cm}^{-1}$ )] were also present. The absorption band at 429 nm in **22a** is similar to the Soret band of porphyrins and porphycenes. The absorptions at longer wavelengths are akin to Q-bands, but with a bathochromic shift compared to porphycenes.

On the other hand, compound **23a** showed a split Soret band at 415 and 433 nm, suggesting lower symmetry ( $C_2$ ), compared to the analogous unsplit Soret band of the high ( $D_{2h}$ ) symmetry **22a**, while the Q-type bands appeared slightly redshifted than those of porphyrins and porphycenes. Interestingly, both **22a** and **23a** dissolved in acids ( $\text{H}_2\text{SO}_4$  and 70%  $\text{HClO}_4$ ) to give a





Fig. 1 NICS analysis of **23a** (A) and **22d** (B). Variation of NICS ppm in **23a** (C) and **22d** (D) with distance  $r$  (Å) from the centre of the macrocyclic plane.



Fig. 2 (A) UV-visible absorption spectra (**20a/22a** in DCM and  $\text{H}_2\text{SO}_4$ ; **21a/23a** in DCM) and (B) cyclic voltammograms of **22a** and **23a** (DCM, electrolyte:  $\text{TBAPF}_6$ ; working electrode: Pt; reference electrode:  $\text{Ag}/\text{AgCl}$ ;  $80 \text{ mV s}^{-1}$ ). Reproduced with permission from ref. 13 and 14. Copyright 2011 and 2012, respectively, The Royal Society of Chemistry.

reddish-violet solution, indicative of the formation of a 20 $\pi$  dicationic species **24/25a** (Scheme 6).<sup>13,14</sup> The UV-visible spectra of **24/25a** in acid solutions showed considerable broadening

of the peaks (Fig. 1), suggesting the formation of antiaromatic species having significantly positive NICS values [ $\delta$  11.29 (**24a**);  $\delta$  19.59 (**25a**)].



Being  $22\pi$  electron macrocycles, **22a** and **22b**<sup>13</sup> are expected to lose two electrons to form the corresponding  $20\pi$  dication. The cyclic voltammograms (Fig. 2) of **22a** and **23a** show two reversible oxidation peaks at 552.6 and 968.2 mV (**22a**) and 418.1 and 970.0 mV (**23a**) (vs. SCE), indicating the formation of  $20\pi$  dicationic species **24a** and **25a** (Scheme 6). Further, the HOMO–LUMO gaps obtained from density functional theory (DFT) calculations in **22a** (2.32 eV) and **23a** (2.06 eV) were quite narrow. Visualization of the charge density isosurfaces of HOMOs and LUMOs revealed  $\pi$ -delocalization over the heteroannulene rings supporting the aromatic character with a greater contribution of heteroatoms to HOMOs compared to LUMOs (Scheme 6).

The single crystal X-ray structures of these porphyrinoids revealed interesting structural features. The four sulphur (or oxygen) atoms of the macrocycle **22a** (or **23a**) lie in one plane (Fig. 3), as were also the four thiophene/furan rings. One of the two sets of sulphur atoms, the ones intercepted by four carbon atoms, are 3.110 Å apart, while the distance between the neighbouring atoms separated by three-carbon atoms is 3.018 Å. Both of these distances were marginally shorter than twice the van der Waals radius of sulphur (3.60 Å). The distance between the two sulphur atoms with a diagonal relationship between each other is 4.333 Å. The planarity of these porphyrinoids is additionally indicated by the torsional angles ( $0^\circ$  and  $3.97^\circ$ ) between the sulphur (or oxygen) atoms and the mean plane of the respective macrocycles. However, in **23a**, the interatomic distance between the two oxygen atoms intercepted by four carbon atoms was 4.590 Å, while the other set intercepted by a two carbon bridge was 2.485 Å apart.

In contrast to the *cis* geometrical arrangement of the two carbon bridge linking two thiophene rings and square arrangement of the four sulphur atoms in **22a**, the oxygen bridged analogue **23a** represented a *trans* geometry of the two carbon bridge connecting the two neighbouring furan rings as well as a rectangular arrangement of the four oxygen atoms.

Consistent with the electron delocalization in the planar aromatic porphyrinoids, bond alteration was not evident in



Fig. 3 Single crystal X-ray structures: side views, top views and stacking patterns of **22a** (A) and **23a** (B). Reproduced with permission from ref. 13 and 14. Copyright 2011 and 2012, respectively, The Royal Society of Chemistry.

either of **22a** and **23a**. The carbon–carbon distances in the thiophene or furan rings of **22a** and **23a**, respectively, showed the bond length relation  $C_\alpha-C_\beta > C_\beta-C_\beta$ , reflecting delocalization in the porphyrin ring. It is worth mentioning that the aromatic tetrathiaporphyrin dication also showed<sup>17</sup> the above bond length relation, in spite of the fact that the four thiophene rings were tilted up and down from the mean molecular plane by  $22.8^\circ$  and  $3.7^\circ$ , respectively. The aromaticity was further verified from the NICS(1) values, which, in contrast to the isolated furan ( $\delta -10.35$  ppm) in **21a**, were significantly negative ( $\delta -20.01$ ,  $-18.65$ ,  $-15.15$  and  $-16.61$  ppm) for the four furan rings of the fully conjugated **23a**.

The molecules of **22a** stacked in a face-to-face pattern along the *c*-axis into columns. The intermolecular  $\pi$ - $\pi$  interactions could be observed as the interplanar distance between the adjacent molecules in one column is 3.526 Å. Likewise, **23a**



Scheme 6 Electrochemical oxidation of **22a/23a** to **24a/25a** and charge density isosurfaces of the HOMOs and LUMOs of **22a** (A: HOMO; B: LUMO) and **23a** (C: HOMO; D: LUMO).



stacked in a standard layer-by-layer herringbone fashion along the *bc*-plane with a tilt angle of  $52.79^\circ$  between the macrocyclic core and the *bc*-plane. Interestingly, the *meso*-phenyl substituents of **22a** and **23a** did not induce puckering of the macrocyclic ring, nor do these affected the aromaticity of the porphyrinoids. However, with the increasing bulk at the *meso*-position, slight macrocyclic ring puckering was observed in other analogues **22c**, **d**, **f**, and **g** (Fig. 4) compared to **22a** and **b** (Fig. 3 and 4).<sup>18,19</sup> However, the aromaticity of these porphyrinoids was intact.

Likewise, the sulphur atoms of **22g** were not coplanar and so are the thiophene rings. In the former, sulphur atoms linked through a *meso*-bridge lied below the twisted macrocyclic plane, compared to the other set. Although the S–S distances of the thiophene rings intercepted by the *meso* or the two carbon bridges were unequal, these were marginally shorter than twice the van der Waals radius of S (3.60 Å).<sup>19</sup>

Comparison of the crystal structures of a number of *meso*-substituted porphyrinoids revealed that hosting bulkier *meso*-substituents resulted in ring puckering, but aromaticity was maintained. Face-to-face crystal packing as in **22g** provides an efficient  $\pi$ -orbital overlap and interplanar distances that facilitate

charge transport. Even molecular twisting/curving did not hamper the transistor behaviour of these porphyrinoids.

### 2.3. Semiconducting behaviour of TPPs and TOPs

Among organic semiconductors,  $\pi$ -conjugated macrocyclic architectures, such as porphyrins and phthalocyanines, have attracted considerable attention due to their promising electronic, optical, and photophysical properties and self-assembling behavior.<sup>19</sup> In recent years, ambipolar (simultaneous p- as well as n-channel charge transport) OFETs have seen unprecedented research activity. This is attributed to their applications in organic circuits and organic light emitting transistors. However, in most cases, ambipolar charge transport was realized by the construction of heterostructures comprising p-type and n-type semiconductors, e.g. bilayer, lateral and bulk heterojunctions. Only in a very few cases, an efficient single component transistor based on an ambipolar charge transport material was reported. An additional advantage of a single component ambipolar charge transport material would be simplification of the fabrication process when two unipolar materials would be replaced with a single ambipolar material.



Fig. 4 Single crystal X-ray structures (A) and stacking patterns (B) of porphyrins **22b–d**, **22f** and **22g** bearing bulkier substituents on the *meso*-phenyl group. Reproduced with permission from ref. 16, 18 and 19. Copyright 2013, 2012 and 2014, respectively, The Royal Society of Chemistry.



TTPs and TOPs were expected to show charge transport owing to the enhanced  $\pi$ - $\pi$  interactions of the  $22\pi$  porphyrins compared to the smaller  $18\pi$  counterparts. In order to demonstrate their application potential in organic electronics, we investigated the semiconducting behaviour of a number of derivatives of **22** and **23** in thin films and single crystal OFET devices. We also explored the possibility of creating a self-assembled “molecular level heterojunction” obtained through co-crystallization of the electron rich **22** with a strong electron acceptor such as 7,7,8,8-tetracyanoquinodimethane (TCNQ) or tetracyanoethylene (TCNE).

As discussed below, **22** and **23** showed substantial p-channel (hole) transport and functioned as p-type semiconductors in thin film OFET devices. The devices displayed good reproducibility under ambient conditions. A good relationship between the molecular structure and transport properties of these aromatic porphyrinoids has been deduced.<sup>20</sup> The charge mobility of different devices was explained in terms of the calculated molecular

reorganization energies and the intermolecular transfer integrals. Further, appending substituents at the *meso*-positions of these porphyrin derivatives provided an understanding of the relationship between the structure and charge transport and the related attributes, such as the device on/off ratio, threshold voltage, *etc.* Before discussing the semiconducting behaviour of these porphyrinoids, a brief introduction to OFET devices and measurement of charge transport behaviour is presented.

**2.3.1. OFET devices and charge transport.** Several review articles that explain the configurations as well as operation of OFET devices are available.<sup>21</sup> Therefore, for the convenience and understanding of the reader, only a brief introduction of these aspects of OFETs is presented herein. A typical OFET comprises a gate electrode, a gate dielectric layer, an organic semiconductor (OSC) layer and a source-drain electrode. Based upon their construction design, OFETs are classified into four categories: bottom-gate/top-contact (BGTC), bottom-gate/bottom-contact (BGBC), top-gate/top-contact (TGTC) and top-gate/bottom-contact



Fig. 5 Schematics of OFET configurations. (A): BGTC; (B): BGBC; (C): TGTC; (D): TCTC (S: source; D: drain; OSC: organic semiconductor; G: gate; Sub: substrate; W: width and L: length of the conducting channel). Typical current–voltage ( $I$ - $V$ ) characteristics using arbitrary  $V_{GS}$  values. (E): output curves (Lr: linear and Sat: saturation regimes); (F): transfer curves ( $V_{th}$ : threshold voltage).



(TGBC) configurations (Fig. 5). The organic semiconductor (OSC) is fixed between the metallic source (S) and drain (D) electrodes. During operation, current is injected into the OSC by S and collected by the D electrode. The gate electrode (G) is separated from the OSC or S/D electrodes by the gate dielectric layer, which, through capacitive coupling, modulates (on/off stages) the conductance of the OSC in the channel region. Fig. 4 also depicts the typical current–voltage ( $I$ – $V$ ) curves (E: output and F: transfer curves), from which the field-effect mobility ( $\mu$ ,  $\text{cm}^2 \text{V}^{-1} \text{s}^{-1}$ ), threshold voltage ( $V_{\text{th}}$ ), and current on/off ratio ( $I_{\text{on}}/I_{\text{off}}$ ) etc. are calculated. The  $I_{\text{on}}/I_{\text{off}}$  ratio represents the ratio of the highest and lowest current values in the sweep of  $V_{\text{GS}}$  at a certain  $V_{\text{DS}}$ .

**2.3.2. OFET device fabrication, characteristics of TTPs and TOPs and structure–property relationships.** The thin films of the TTPs and TOPs, purified by vacuum sublimation, were prepared by vacuum deposition on octadecyltrichlorosilane (OTS) modified or bare  $\text{SiO}_2$ . Atomic force microscopy (AFM) and powder X-ray diffraction (PXRD) (Fig. 6) were used for characterization and study of the surface morphology of the thin films. Variation of the substrate temperature showed a significant influence on the morphology, crystallinity and the corresponding transport properties of the thin film transistors.

Thin films of **22a** and **22b** were highly crystalline and the first intense reflection was observed at  $2\theta = 5.43$ ,  $5.09$  and  $5.111$  (Fig. 6) for **22a**, **22b** and **22c**, respectively, corresponding to



**Fig. 6** (A) Schematic of the BGTC thin film OFET devices of **22a–c**; (B) X-ray diffraction patterns of the thin films of **22a** deposited on  $\text{SiO}_2/\text{Si}$  (BARE) and  $\text{OTS}/\text{SiO}_2/\text{Si}$  substrates at different temperatures; (C) AFM images ( $2 \times 2 \mu\text{m}$ ) of  $50 \text{ nm}$  thick films of **22a** (a: BARE  $T_s = 25^\circ\text{C}$ ; b: OTS  $T_s = 25^\circ\text{C}$ ; c: OTS  $T_s = 60^\circ\text{C}$ ); **22b** (d: BARE  $T_s = 25^\circ\text{C}$ ; e: OTS  $T_s = 25^\circ\text{C}$ ; f: OTS  $T_s = 60^\circ\text{C}$ ); **22c** (g: BARE  $T_s = 25^\circ\text{C}$ ; h: OTS  $T_s = 25^\circ\text{C}$ ; i: OTS  $T_s = 60^\circ\text{C}$ ); (D) normalized UV-vis absorption spectra of thin films of **22a–c** at room temperature; (E) transfer and (F) output characteristics of the thin film OFET devices (deposited on an OTS treated  $\text{SiO}_2/\text{Si}$  substrate ( $T_s = 25^\circ\text{C}$ )) based on **22a**. Reproduced with permission from ref. 13. Copyright 2011, The Royal Society of Chemistry.



*d*-spacings of 1.62, 1.73 and 1.73, which corresponded to the molecular lengths along the longer axis (1.86 Å, 2.02 Å and 2.00 Å nm for **22a–c**, respectively). We deduced that the porphyrins were aligned on the substrate with their long axes inclined at angles of 60.6, 59.0 and 59.0 degrees, respectively. This was in stark contrast to the *meso*-unsubstituted **5**, which aligned nearly perpendicular to the substrate.<sup>22,23</sup> Furthermore, the UV-visible absorption spectra of the thin films were identical to the solution spectrum (Fig. 6).

The thin film OFET devices of **22a–c** revealed them to be p-type semiconductors (Fig. 6). The highest performance (field-effect mobility) was shown by **22b** in thin film devices deposited on OTS-modified SiO<sub>2</sub> at a substrate temperature of 25 °C. It recorded field-effect mobility as high as 0.65 cm<sup>2</sup> V<sup>-1</sup> s<sup>-1</sup> and the value was among the highest of thin film OFETs.

Compared to the *meso*-unsubstituted derivative **5**, the *meso*-phenyl substituents (electron-withdrawing as well as electron-donating, *vide infra*) significantly improved the transport properties of these materials. This could presumably be attributed to the change of the molecular stacking pattern of **22a–c** in the thin films. The substituents at the *meso*-aryl groups modulated the charge transport properties, especially the current on/off ratios, of the thin film devices. The superior charge transport was attributed to the extended  $\pi$ -conjugation of these cyclic conjugated molecules, which lowers the reorganization energy and leads to enhanced intermolecular  $\pi$ - $\pi$  overlap. Compared with **5**, which showed herringbone (edge-to-face) stacking in

the solid state, the *meso*-substituents in **22** (and **23**, *vide infra*) altered the molecular stacking pattern to face-to-face or shifted face-to-face and significantly improved the charge transport as well as switching properties of the materials based on thin films. Interestingly, the charge (hole current) transport values of these porphyrin derivatives were considerably superior to those of the corresponding  $\alpha$ -oligofurans (mobility: 0.05–0.066 cm<sup>2</sup> V<sup>-1</sup> s<sup>-1</sup>) and  $\alpha$ -oligothiophenes (0.09 cm<sup>2</sup> V<sup>-1</sup> s<sup>-1</sup>).<sup>24</sup>

Thin-film OFETs of **23a** and **23b** were fabricated on OTS or polymethylmethacrylate (PMMA)/SiO<sub>2</sub>/Si substrates in a BGTC configuration using Au source and drain electrodes. The UV-visible absorption spectrum of the thin films (Fig. 7A) corresponded to the solution spectra. The morphology of the thin films changed with temperature. Upon increasing the temperature from 20 °C to 60 °C, the grain size increased and the films turned more ordered; however, at 100 °C, cracks appeared in the films (Fig. 7B). The best charge transport (Fig. 7C and D) with a mobility as high as 0.40 cm<sup>2</sup> V<sup>-1</sup> s<sup>-1</sup> was observed on thin films of **23a** deposited on OTS modified SiO<sub>2</sub> at a substrate temperature of 60 °C. The more positive value of the threshold voltage ( $V_{th}$ ), observed for the OTS modified devices, was attributed to the assembly of charges on the OTS surface during the operation. The device of **23a** based on a PMMA surface modified SiO<sub>2</sub>/Si substrate yielded a rather higher on/off ratio and a favorable  $V_{th}$ .

Compound **22d** crystallized in an orthorhombic unit cell and, unlike **22a**, the sulphur atoms of the porphyrin macrocycle are not in the same plane. The two sulphur atoms linked



Fig. 7 (A) Normalized UV-visible absorption spectra of thin films of **23a** and **23b** at room temperature; (B) AFM images of 50 nm thick films deposited on an OTS modified SiO<sub>2</sub>/Si substrate of **23a** (5 × 5 μm) at 25 °C (a), 60 °C (b) and 100 °C (c) and **23b** (2 × 2 μm) at 25 °C (d), 60 °C (e) and 100 °C (f); (C) transfer and (D) output characteristics of the thin film OFET devices deposited on an OTS treated SiO<sub>2</sub>/Si substrate ( $T_s = 60$  °C). Reproduced with permission from ref. 14. Copyright 2012, The Royal Society of Chemistry.



through the *meso*-bridge are positioned below the plane of the otherwise twisted macrocycle. The set of sulphur atoms intercepted by a four carbon bridge is well above the mean macrocyclic plane. The shifted face-to-face stacking pattern in the layered supramolecular structure and the interplanar distance (3.4–3.6 Å) between the adjacent molecules suggested intermolecular  $\pi$ - $\pi$  interactions and the consequent electron transport.

The thin films (50 nm) of **22d** and **22e** were vacuum-deposited on OTS treated SiO<sub>2</sub>/Si wafers by thermal evaporation under a pressure of  $8 \times 10^{-4}$  Pa. The deposition rate was gradually increased from  $0.1 \text{ \AA s}^{-1}$  to  $0.4 \text{ \AA s}^{-1}$  up to the first 20 nm and then maintained  $0.5 \text{ \AA s}^{-1}$  until the thickness of the film was 50 nm. The films deposited at a substrate temperature of 20 °C essentially consisted of small grains, which grew in size at 60 °C, and resulted in a more ordered film. However, increasing the substrate temperature to 100 °C, the films cracked and lamellar crystalline grains were observed. In contrast to the thin films of **22a–b**, no obvious diffraction peaks could be observed in the XRD patterns of **22d** and **22e**, attesting to the amorphous character of the thin films.

The band gap of **22d** and **22e** was estimated to be 1.57 eV from the absorption onsets. The HOMO levels of **22d** and **22e** were estimated to be  $-5.04$  and  $-4.98$  eV, respectively, by CV measurements which were comparable to the HOMO level of gold ( $-4.9$  eV), suggesting an effective hole mobility between the electrode and the semiconductor leading to improved device performance. Visualization of the HOMOs and LUMOs (Fig. 8) of **22d** and **22e** revealed  $\pi$ -delocalization over the porphyrin macrocycle supporting the observed aromatic character and greater contribution of sulphur atoms to HOMOs compared to LUMOs. The AFM morphologies of the thin (50 nm) films of **23d** and **23e** vacuum-deposited on OTS treated SiO<sub>2</sub>/Si wafers are shown in Fig. 8. The films essentially consisted of small grains when the substrate temperature was 20 °C. However, at elevated temperature (60 °C), these grains turned bigger in size and resulted in more ordered thin films on the OTS/SiO<sub>2</sub>/Si substrate. Finally, when the substrate temperature was further increased to 100 °C, lamellar crystalline grains were observed. However, no obvious diffraction peaks could be observed in the XRD patterns, which indicated the amorphous character of these thin films.

Devices of **23d** fabricated at 100 °C exhibited the best OFET performance ( $\mu = 0.23 \text{ cm}^2 \text{ V}^{-1} \text{ s}^{-1}$ ) with a much improved on/off ratio of  $5 \times 10^5$ . Interestingly, the mobility of these devices did not change significantly upon exposure to air even up to ten days, although the on/off ratio decreased by one order of magnitude. Small molecule based amorphous thin films with a relatively high mobility are still rare. We believe that the extended  $\pi$ -conjugation in these porphyrinoids contributes to efficient intermolecular coupling in the thin films lacking molecular structural ordering.

As a logical extension of this work, we planned to investigate the influence of steric bulk at the *meso*-positions of TTPs. Thus, we synthesized porphyrins **22f–h** bearing *p*-Et-C<sub>6</sub>H<sub>4</sub>, *p*<sup>-1</sup>Pr-C<sub>6</sub>H<sub>4</sub>, and *p*<sup>-4</sup>Bu-C<sub>6</sub>H<sub>4</sub> substituents at 5- and 16-positions.<sup>19</sup> We observed that the solubility of these porphyrinoids was highly dependent on the *meso*-substitution. The solubility significantly decreased from **22f** to **22h** bearing *p*-Et-C<sub>6</sub>H<sub>4</sub>, *p*<sup>-1</sup>Pr-C<sub>6</sub>H<sub>4</sub>, and



Fig. 8 The electron densities of the HOMO (A) and LUMO (B) of **23d** (isosurface value = 0.04); (C) AFM images: 50 nm thick films ( $2 \times 2 \mu\text{m}$ ) of **23d** deposited on an (a) OTS/SiO<sub>2</sub>/Si substrate,  $T_s = 20$  °C; (b) OTS/SiO<sub>2</sub>/Si substrate,  $T_s = 60$  °C; and (c) OTS/SiO<sub>2</sub>/Si substrate,  $T_s = 100$  °C; and 50 nm thick films ( $5 \mu\text{m} \times 5 \mu\text{m}$ ) of **23e** deposited on an (d) OTS/SiO<sub>2</sub>/Si substrate,  $T_s = 20$  °C; (e) OTS/SiO<sub>2</sub>/Si substrate,  $T_s = 60$  °C; and (f) OTS/SiO<sub>2</sub>/Si substrate,  $T_s = 100$  °C. Reproduced with permission from ref. 18. Copyright 2012, The Royal Society of Chemistry.

*p*<sup>-4</sup>Bu-C<sub>6</sub>H<sub>4</sub> substituents at the two *meso*-positions. This provided a guideline for designing *meso*-substituted porphyrins with the possibility of solution processible OFETs.

Among **22f–h**, the thin film OFETs (Fig. 9) of **22f** exhibited the highest OFET performance at 100 °C. While the hole mobility averaged at  $0.32 \text{ cm}^2 \text{ V}^{-1} \text{ s}^{-1}$  (100 °C), the on/off ratio was  $1 \times 10^6$  (25 °C). It also showed a very favourable threshold voltage ( $V_T$ ) of  $-14$  V.

Interestingly, a comparison of the field-effect mobility (Table 1) of these porphyrinoids revealed that substituting a phenyl group at the *meso* position of 5 to produce **22a** (Ar = Ph) and **22b** (Ar = *p*-Me-Ph) led to nearly 12.5- and 31.5-fold, respectively, increases in the field effect mobility. This is attributed to the difference in the crystal packing pattern, leading to effective  $\pi$ - $\pi$  interactions. Further, substituting the *meso*-phenyl group with *p*-Et, *p*<sup>-1</sup>Pr, and *p*<sup>-4</sup>Bu to produce **22f**, **22g**, and **22h**, respectively, led to significant deterioration of the field-effect mobility. The molecules of these compounds were arranged in a shifted face-to-face fashion in the crystal packing structures. Likewise, a *p*-F, *p*-Cl or *m*-Cl substituent on the *meso*-phenyl group led to a decrease in the field-effect mobility compared to the unsubstituted Ph **22a** or *p*-Me-Ph **22b**. Except for **5** (*meso*-phenyl) and **22b/22f** (*meso-p*-Me-Ph/*p*-Et-Ph), the thin films of all TTPs were amorphous (Table 1), which seems to be a distinctive feature affecting the field-effect mobility of this class of porphyrinoids.

The oxygen analogue **23a** (*meso*-Ph), due to a layered herringbone crystal packing, seems to maintain rather amorphous





Fig. 9 (A) AFM images ( $5 \times 5 \mu\text{m}$ ) of 50 nm thick films of **22f–h**, (a, d and g)  $T_s = 25^\circ\text{C}$ ; (b, e and h)  $T_s = 60^\circ\text{C}$ ; (c, f and i)  $T_s = 100^\circ\text{C}$ . (B/D) Transfer and (C/E) output characteristics of the thin film OFET devices of **22f/22g** (deposited on OTS treated  $\text{SiO}_2/\text{Si}$  substrate ( $T_s = 25^\circ\text{C}$ )). Reproduced with permission from ref. 19. Copyright 2014, The Royal Society of Chemistry.

thin films and yielded high field-effect mobility (Table 1), while **23b** (*meso-p*-Me-Ph) showed less, yet good field-effect mobility.

To examine the relationship between the structure and charge transport behaviour of these porphyrinoids, with an eye on the rational design of organic semiconductors from this category of compounds, single crystal organic field effect transistors (SCOFETs) based on representative members (**22a–c**) of these porphyrinoids were fabricated and their charge transport behaviour was analysed and corroborated by theoretical calculations of their molecular reorganization energies and the maximum intermolecular transfer integrals. Fabricating SCOFET devices ensured elimination of possible defects and morphological

issues of the thin film devices as discussed in the preceding sections.

While the porphyrin ring of **22a**, having *meso*-Ph groups maintaining coplanar conformation with S atoms and four thiophene rings, deviates from the mean plane only by less than  $0.1 \text{ \AA}$  (Fig. 3), the deviation in **22b** having *p*-Me-Ph groups at the *meso* positions was greater (dihedral angle of  $3\text{--}4^\circ$ ) (Fig. 3). In **22c**, however, the bulkier *p*-Cl-Ph groups at the *meso* positions made it to adopt significantly twisted conformation (dihedral angle of  $13.7\text{--}22.2^\circ$ ) (Fig. 4). These compounds showed face-to-face packing in the crystals, which was distinctively different from the dimerized herringbone packing of the *meso*-unsubstituted analogue **5**.<sup>23</sup>



Table 1 Summary of the characteristics of the thin film OFET devices of TTPs and TOPs

	Ar	Crystal packing mode	Thin film type	$T_{\text{sub}}$ (°C)	$\mu^a$	$I_{\text{on}}/I_{\text{off}}$	$V_T$ (V)
5	—	Edge-to-face <sup>b</sup>	Crystalline	18	0.02 <sup>22</sup>	10 <sup>3</sup>	—
22a	Ph	Face-to-face	Crystalline	25	0.29 <sup>13</sup>	1.34 × 10 <sup>3</sup>	−12.9
22b	<i>p</i> -Me-Ph	Slipped face-to-face	Crystalline	25	0.63 <sup>13</sup>	3 × 10 <sup>2</sup>	−7.47
22f	<i>p</i> -Et-Ph	Face-to-face	Crystalline	100	0.32 <sup>19</sup>	6 × 10 <sup>4</sup>	−14.0
22g	<i>p</i> <sup>1</sup> -Pr-Ph	Shifted face-to-face	Amorphous	25	0.0014 <sup>19</sup>	3 × 10 <sup>4</sup>	3.0
22h	<i>p</i> <sup>4</sup> -Bu-Ph	Shifted face-to-face	Amorphous	25	0.0087 <sup>19</sup>	9 × 10 <sup>2</sup>	−5.8
22e	<i>p</i> -F-Ph	Shifted face-to-face	Amorphous	100	0.012 <sup>18</sup>	2.4 × 10 <sup>5</sup>	−56.1
22c	<i>p</i> -Cl-Ph	Shifted face-to-face	Amorphous	60	0.0245 <sup>18</sup>	3.03 × 10 <sup>4</sup>	−50.1
22d	<i>m</i> -Cl-Ph	Shifted face-to-face	Amorphous	100	0.23 <sup>18</sup>	5.27 × 10 <sup>5</sup>	−17.1
23a	Ph	Layer by layer <sup>c</sup>	Amorphous	60	0.40 <sup>16</sup>	3.5 × 10 <sup>3</sup>	−20
23b	<i>p</i> -Me-Ph	Layer by layer <sup>c</sup>	Amorphous	100	0.11	1.0 × 10 <sup>2</sup>	−24.4

<sup>a</sup> cm<sup>2</sup> V<sup>−1</sup> s<sup>−1</sup>. <sup>b</sup> Dimers arranged in a herringbone fashion. <sup>c</sup> Herringbone.

The theoretical calculations on the two structural isomers of these compounds, namely, the parallel and staggered forms (*meso* substituents w.r.t. the macrocyclic ring), revealed only a small stabilization (10 meV) of the latter relative to the former, which meant that **22a** and **b** may adopt a parallel conformation, whereas **22c** would prefer a staggered conformation. However, the HOMOs and LUMOs of **22a–c** (Fig. 10) are mainly localized on the cyclic conjugated pathway, negating the effect of the *meso*-Ph substituents on the HOMO and LUMO charge densities. The stability of these porphyrins was demonstrated from the calculated ionization energies (both adiabatic and vertical). These were in the range (from 5.68 eV to 6.78 eV) recorded for air stable p-channel materials.<sup>25</sup> The calculated reorganization energy for both parallel and staggered conformations of the compounds revealed a greater influence of the molecular conformation than the modification of the *meso*-substituent. The latter however seems to be the major factor affecting the charge transport properties through alteration of the molecular packing and transfer integrals.

The SCOFETs (Fig. 11) of **22a–c** exhibited typical p-type characteristics under ambient conditions. Single crystal (top contact) devices of **22a** fabricated using the drop casting method showed the highest mobility of 0.7 cm<sup>2</sup> V<sup>−1</sup> s<sup>−1</sup> with

an average mobility of 0.4 cm<sup>2</sup> V<sup>−1</sup> s<sup>−1</sup>, while the field-effect mobility was in the range of 0.03 to 0.4 cm<sup>2</sup> V<sup>−1</sup> s<sup>−1</sup> for **22b**, and for **22c** the mobility was in the range of 0.005 to 0.2 cm<sup>2</sup> V<sup>−1</sup> s<sup>−1</sup>.<sup>16</sup>

Based on the crystal structures of **22a–c** and the theoretically calculated (site energy correction method: PW91PW91/6-31G\* level)<sup>26</sup> transfer integrals, the major intermolecular charge transfer pathways are shown in Fig. 12. It is obvious that **22a** displayed one-dimensional transport character along the *c*-axis (*i.e.* along P3 and P4). The larger intermolecular distance along the other pathways (P1 and P2) yielded very small transfer integrals. However, **22b** and **22c** displayed two-dimensional transport behaviour, although charge transfer integrals along all directions were small. Further, since **22c** adopts twisted conformation due to the presence of bulky *p*-Cl-Ph groups at 5- and 15-positions,  $\pi$ - $\pi$  stacking is inhibited. Consequently, the charge transport integrals along P3 and P4 were unusually small (−1.803 and −9.362 meV). The smaller transfer integrals have been rationalized in terms of molecular displacement along the molecular axis in the dimeric arrangement and the shape of HOMOs that do not favour molecular overlap. This analysis further suggested that the reorganization energy is a superior contributor than the intermolecular electronic coupling (transfer integrals) for these classes of porphyrinoids.

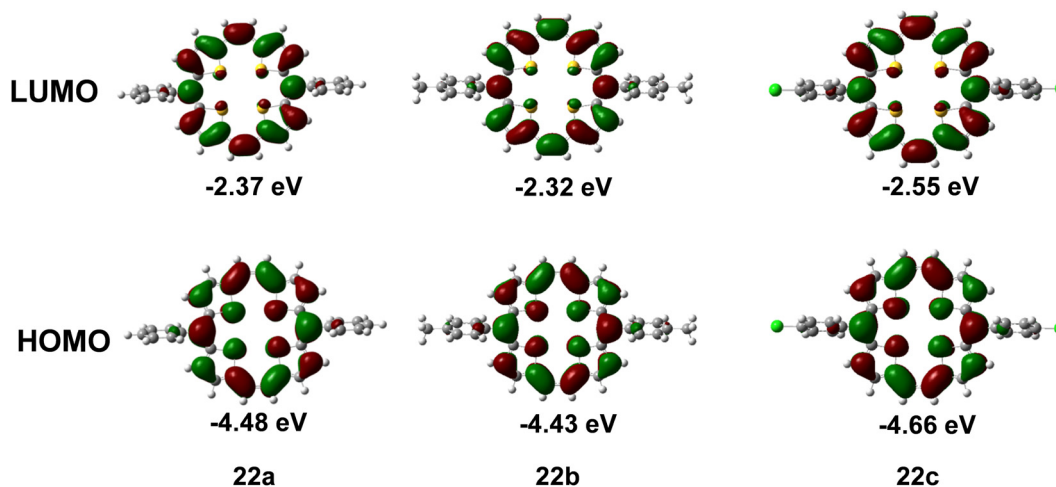


Fig. 10 HOMO and LUMO energies of **22a–c**.





**Fig. 11** (A) SEM images of an individual wire (a), ribbon (b) and plate (c) of **22a–c**, respectively; (B) optical images (a, b and c) of the SCOFET devices of **22a–c**, respectively; (C–E) powder diffraction patterns of the wires, ribbons and plates of **22a–c**, respectively. The peaks are indexed with lattice constants of the bulk crystals; (F) schematic structure of a BGTC SCOFET device. Reproduced with permission from ref. 16. Copyright 2013, The Royal Society of Chemistry.

Thus, the nature of the substituents at the 5- and 15-positions of the TTPs play a significant role in molecular packing (from herringbone to face-to-face) and  $\pi$ - $\pi$  stacking in addition to the solubility, crystallinity and thus the performance of SCOFET devices. Suffice to say, we have demonstrated

that chemical modification at the *meso*-position of TTPs/TOPs constitutes a powerful tool in designing efficacious organic semiconductors. In the succeeding section, we have presented our work on ambipolar charge transport materials.





Fig. 12 Schematics depicting the distances of the centroids and major transfer integrals between the two molecules of **22a–c** (A–C, respectively). Reproduced with permission from ref. 16. Copyright 2013, The Royal Society of Chemistry.

#### 2.4. Ambipolar charge transport materials based on TTPs

Materials wherein both p-type and n-type channels transport holes and electrons, simultaneously, are called ambipolar charge transport materials. These are of tremendous significance because of their potential applications in complementary-like circuits, organic light-emitting transistors, *etc.*<sup>27</sup> Despite the significant progress in unipolar (p- or n-type) semiconductors, designing unimolecular compounds that show efficient ambipolar transport behaviour (both stable p-type and n-type) under ambient conditions is still a challenge. Unimolecular ambipolar charge transport materials avoid the complexity in the fabrication processes of ambipolar devices where two unipolar (p- and n-type) materials are used. Alternatively, ambipolar transistors have been fabricated using heterostructures with p-type and n-type

semiconductors as exemplified by bilayer heterojunctions,<sup>28</sup> bulk heterojunctions<sup>29</sup> and lateral heterostructures.<sup>30a,b</sup> This approach allowed construction of heterojunctions with molecular level self-assembly through cocrystallization of p-type and n-type organic semiconductors. Recently, theoretical evaluation of the superexchange couplings for donor–acceptor cocrystals and copolymers has been introduced and rationalized to elucidate the design principles to obtain high-mobility organic semiconductors.<sup>30c</sup>

In view of the superior p-type semiconducting behaviour of **22** as discussed in the preceding sections, we considered creating molecular level heterojunctions through self-assembling of the donor–acceptor (D–A) dyads using **22a** as a p-type component in combination with an established n-type component such as tetracyanoquinodimethane (TCNQ)<sup>31</sup> or fullerenes (C<sub>60</sub> and C<sub>70</sub>).<sup>32</sup>



Using cocrystals of these dyads would have also cultivated the advantage of SCOFETs, which have been proven to be one of the most powerful tools for probing the relationship between intrinsic electrical transport properties, molecular structures and their stacking patterns. The superiority of such devices lies in the fact that there are fewer defects and morphological issues compared to thin film devices.<sup>33</sup>

The donor component **22a** with a HOMO energy level of  $-4.88$  eV showed a hole mobility of  $0.29$   $\text{cm}^2 \text{V}^{-1} \text{s}^{-1}$  (Table 1) in thin film OFET devices. On the other hand TCNQ is an efficient n-type semiconductor with a high electron mobility of up to  $1.6$   $\text{cm}^2 \text{V}^{-1} \text{s}^{-1}$  in single crystals.

The single crystal of **22a**-TCNQ was obtained by slow evaporation of a chlorobenzene solution of a 1:1 mixture of **22a** ( $1$   $\text{mg mL}^{-1}$ ) and TCNQ. In the molecular structure of **22a**-TCNQ (Fig. 13A), **22a** adopted a nearly coplanar structure with the four S atoms deviating from the mean plane by  $0.05$ ,  $0.07$ ,  $-0.05$  and  $-0.07$ , respectively. The dihedral angle between the

molecular planes of **22a** and TCNQ was of the order of  $3.46(4)^\circ$ . Further, the intermolecular distance between the two components of the crystal was  $3.4$  Å, which was slightly shorter than the typical van der Waals interaction, while a strong non-bonding interaction between the two components was  $3.158$  Å. Further, in the solid state of the complex, **22a** and TCNQ stacked alternatively (Fig. 13B) into a one-dimensional column structure along the *a*-axis. The face-to-face stacking allowed overlap of TCNQ with half of the plane of **22a**, leading to lateral interactions between **22a** and TCNQ in adjacent columns, comprising conducting channels for both holes and electrons, respectively. The powder X-ray diffraction pattern of the micro-ribbons (Fig. 12C) revealed intense peaks (001 and 002). A very interesting feature of the **22a**-TCNQ complex was the lack of charge transfer between the two constituting components. This was inferred from the stretching frequency of CN of TCNQ in the complex ( $2224$   $\text{cm}^{-1}$ ), which matched favourably with the pristine, neutral TCNQ ( $2223$   $\text{cm}^{-1}$ ), and from the geometry of TCNQ in the



**Fig. 13** (A) Molecular structure of the **22a**-TCNQ cocrystal with 50% probability ellipsoids; (B) alternative stacking pattern of **22a** and TCNQ; (C) optical images of a single and several cocrystal micro-ribbons of **22a**-TCNQ obtained by the drop-casting method through evaporation of a drop of a mixture of **22a** and TCNQ in chlorobenzene on an OTS/SiO<sub>2</sub>/Si substrate; (D) powder diffraction pattern of the micro-ribbons; (E) optical image of the SCOFET BGTC device of **22a**-TCNQ with an individual single crystal; (F) transfer and (G) output characteristics of the device of **22a**-TCNQ (channel length,  $L = 43.7$   $\mu\text{m}$ , channel width,  $W = 6.0$   $\mu\text{m}$ ). Reproduced with permission from ref. 31. Copyright 2012, Wiley-VCH.



complex. Thus, the ratio of the three conjugating bonds  $c/b + d$  (Fig. 13A) for the **22a**-TCNQ complex as well as neutral TCNQ was identical (0.476).

The devices of **22a**-TCNQ exhibited ambipolar behaviour with stable balanced hole mobility of  $0.04 \text{ cm}^2 \text{ V}^{-1} \text{ s}^{-1}$  and electron mobility of  $0.03 \text{ cm}^2 \text{ V}^{-1} \text{ s}^{-1}$  in ambient atmosphere and represented a novel and easy-to-process approach for realizing ambipolar transport. Further, complementary metal-oxide-semiconductor (CMOS)-like inverters have been constructed by using two identical transistors built on a single crystal using a common gate (Si) for both the transistors. The inverter worked with a maximum gain of 10. The **22a**-TCNQ cocrystal constituted the first example of a neutral, D-A type self-assembled complex that displayed a balanced ambipolar charge transport and application in CMOS-like circuits based on micro-scale crystals. Since this mixed D-A stacking complex represented a heterostructure with molecular level order, it was termed as a “molecular level heterojunction”.

The superiority of the electrical and optical properties of the self-assembled D-A dyad of **22a**-TCNQ, and the distinctive electronic and photophysical properties of TTPs led us to investigate relationship between the electrical performance and molecular structures. We reported<sup>32</sup> the first example of formation of self-assembled D-A cocrystals of the donor **22a** with the fullerene ( $\text{C}_{60}$  and  $\text{C}_{70}$ ) acceptor as a two-dimensional (2D) segregated alternating layer structure, which displayed ambipolar charge transport as well as photoresponsivity. Additionally, the crystal structures of the D-A dyads provided an unambiguous understanding of the relationship between the solid state molecular packing and charge-transport properties.

The molecular structures (Fig. 14) of the crystals of **22a**- $\text{C}_{60}$  and **22a**- $\text{C}_{70}$  revealed a slight deviation of the planarity of **22a**

in a way that half of the porphyrin was bent up, while the other half was bent down which allowed fitting of the curvature of the fullerenes. Both **22a** and fullerene partners were stacked in linear column structures supported by nonbonding interactions between the D and A components. For **22a**- $\text{C}_{60}$ , both the components are packed, individually, into layers along the  $bc$  plane. A tetragonal array with a centroid distance of  $10.02 \text{ \AA}$  was formed by the spheroidal  $\text{C}_{60}$ , which was in fact larger than the distance ( $9.94 \text{ \AA}$ )<sup>34</sup> in the crystal of pristine  $\text{C}_{60}$ . Further, the shortest C-C contacts between the two molecules of  $\text{C}_{60}$  were  $3.325$ – $3.388 \text{ \AA}$ . On the other hand, in the layer of the donor **22a**, the shortest C-C distance was  $3.315 \text{ \AA}$ , which is less than twice the van der Waals radius of carbon ( $3.40 \text{ \AA}$ ). Such intermolecular distances in the layers of both **22a** and  $\text{C}_{60}$  suggested strong  $\pi$ - $\pi$  interactions conducive to the transport of holes and electrons in the individual layers of **22a** and  $\text{C}_{60}$ . In the case of crystals of **22a**- $\text{C}_{70}$  a similar layer structure was observed. The single crystal structure analysis provided a good opportunity to understand the relationship between the molecular structure and charge transport and separation properties.

Parallelogram shaped D-A cocrystals of **22a** with  $\text{C}_{60}/\text{C}_{70}$  (Fig. 15A and B) representing alternating layer-by-layer packing were obtained by the drop-casting method. The crystal structures of these cocrystals were identical to their bulk counterparts as revealed by their X-ray diffraction patterns (Fig. 15C and D). The strong peak at  $6.71^\circ$  in the XRD pattern of **22a**- $\text{C}_{60}$  corresponded to a  $d$  spacing of  $1.30 \text{ nm}$ , which was consistent with the  $a$ -axis, meaning thereby that the crystals grew with the  $bc$  plane perpendicular to the substrate, while in the case of **22a**- $\text{C}_{70}$ , the growth of the crystal was along the  $ab$  plane parallel to the substrate. The BGTC devices (Fig. 15E) of microcrystals of these D-A dyads showed ambipolar charge transport behaviour. The saturated electron and hole mobilities were  $0.01 \text{ cm}^2 \text{ V}^{-1} \text{ s}^{-1}$  and  $0.3 \text{ cm}^2 \text{ V}^{-1} \text{ s}^{-1}$ , respectively, for the nanosheets of **22a**- $\text{C}_{60}$ , while for **22a**- $\text{C}_{70}$ , a more balanced ambipolar transport behaviour with electron and hole mobilities of  $0.05 \text{ cm}^2 \text{ V}^{-1} \text{ s}^{-1}$  and  $0.07 \text{ cm}^2 \text{ V}^{-1} \text{ s}^{-1}$ , respectively, was noticed.<sup>32</sup> Further, the latter device showed a sensitive photoresponse<sup>35</sup> (Fig. 15F), when a large  $V_G$  was applied. Upon the application of large  $V_G$ , more charges accumulate in the conducting channel. The light responsivity of the device under an optical power of  $5.51 \text{ mW cm}^{-2}$  was  $300 \text{ A W}^{-1}$ .<sup>32</sup>

As discussed earlier, the reorganization energy and electronic coupling ( $\lambda$ ) are the two important factors that influence the charge-transport properties of organic semiconductors. The charge transfer decreases with reorganization energy and increases with electronic coupling. The calculated reorganization energies of  $\text{C}_{60}$  and  $\text{C}_{70}$  were  $135$  and  $142 \text{ meV}$ , respectively, while for **22a** it was  $201 \text{ meV}$ .

The electron and hole transport pathways of the fullerene and **22a** components were similar, and for **22a**- $\text{C}_{60}$ , these are depicted in Fig. 16. The calculated effective transfer integrals were  $34$  and  $12.3 \text{ meV}$ , respectively, for electrons and holes, along all pathways indicating isotropy of both the charges in **22a**- $\text{C}_{60}$ . However, in **22a**- $\text{C}_{70}$ , the effective integrals for electrons were  $34 \text{ meV}$  for paths P1 and P2, while for P3 and



Fig. 14 (A and C) ORTEP drawings of the asymmetric units with thermal ellipsoids set at 50% probability level and (B and D) stacking patterns viewed along the  $b$ -axis for **22a**- $\text{C}_{60}$  (A and B) and **22a**- $\text{C}_{70}$  (C and D). Reproduced with permission from ref. 32. Copyright 2013, The American Chemical Society.





Fig. 15 Optical micrographs of self-assembled **22a**-C<sub>60</sub> (A) and **22a**-C<sub>70</sub> (B); XRD patterns of **22a**-C<sub>60</sub> (C) and **22a**-C<sub>70</sub> (D); (E) optical image of the single crystal BGTC devices; (F) photocurrent responses of the **22a**-C<sub>70</sub> microcrystal based transistor under light irradiation. Reproduced with permission from ref. 32. Copyright 2013, The American Chemical Society.

P4 these were 27.9 meV. Likewise, for holes, only P1 and P3 showed significant coupling. This indicates a higher electron transport compared to hole transport, which was in contrast to the experimental values ( $0.01 \text{ cm}^2 \text{ V}^{-1} \text{ s}^{-1}$  and  $0.3 \text{ cm}^2 \text{ V}^{-1} \text{ s}^{-1}$ , respectively, for electron and hole mobilities), especially in **22a**-C<sub>60</sub>. This has been attributed to the greater sensitivity of electron transport to traps at the semiconductor-dielectric interface and internal defects in the devices.<sup>36</sup>

### 3. Nonlinear optical behaviour of meso-substituted TTPs and TOPs

Nonlinear optical (NLO) materials have attracted considerable attention owing to their extensive applications in data storage,<sup>37a</sup>

light modulation, optical switching,<sup>37b,c</sup> optical limiting,<sup>37d</sup> sensors,<sup>37e</sup> etc. Therefore, finding new and stable NLO materials with strong NLO response constitutes an important area of investigation. TTPs/TOPs exhibit high stability owing to extensive conjugation and rich redox properties; therefore, these could be recognized as promising NLO materials. A number of reports are available on the third order NLO properties of porphyrins which could be tuned by metal complexation,<sup>13,14</sup> functionalization and  $\pi$ -conjugation.<sup>37f,g</sup> Owing to centrosymmetric nature,<sup>37h</sup> however, the second order NLO properties of porphyrins and their derivatives have rarely been investigated.

In continuation of our interest in developing NLO active materials,<sup>38</sup> we initially recorded<sup>39</sup> the excited state cross sections of photostable **22a**, **22c** and **22g** in DCM using the open aperture Z-scan technique using 527 nm and 100 ns laser





Fig. 16 Charge hopping pathways of the (A) acceptor ( $C_{60}$ ) and (B) donor (**22a**) components in the individual molecular layers. Reproduced with permission from ref. 32. Copyright 2013, The American Chemical Society.

pulses at a low repetition rate of 250 Hz. Since the compounds were almost transparent at 527 nm, correction for resonance enhancement was not needed. While the excited state absorption cross section  $\sigma_{\text{ex}}$  values were calculated using a simple five-level model (Fig. 17), the ground state absorption cross section  $\sigma_{\text{gr}}$  values were calculated from the linear absorption coefficient.<sup>39</sup> Very high cross-section ratios ( $\sigma_{\text{ex}}/\sigma_{\text{gr}}$ ) of 250, 498 and 197 (Table 2) were obtained for **22a**, **22c** and **22g**, respectively.

The HOMO–LUMO gap of these  $22\pi$  porphyrins is marginally smaller in **22c** compared to **22a** and **22c** due to stabilization of LUMOs due to the substitution of the *meso*-position with the

electron-withdrawing *p*-Cl- $C_6H_4$  group. Consequently, the larger molecular polarizability and hence global softness (as inferred from the inverse of molecular hardness,  $\eta$ ) results in the observed higher excited state cross-section value. Further, the excited state decay profiles (Table 2) of **22a**, **22c** and **22g** yielded the lowest singlet excited state lifetimes of 170, 1500 and 140 ps, respectively (Table 2), which correlated well with the excited state cross-section values. A large (1500 ps) singlet excited state lifetime of **22c** indicated slow excited state relaxation, *i.e.* a decelerated internal conversion between  $S_1$  and  $S_0$  states in spite of a marginally lower optical band gap. Porphyrins **22a**, **22c** and **22g** demonstrated very good optical limiting potential (Fig. 17) at 527 nm using dilute (1 mM) solution excluding the effect of any aggregation. The fluence threshold was found to be 0.310, 0.53 and 0.217  $J\text{ cm}^{-2}$ , respectively, for **22a**, **22c** and **22g**, which were quite low. Thus these porphyrins showed reverse saturable absorption (RSA), which was attributed to excited state absorption.

The observed nonlinearities in these porphyrins are attributed to the population redistribution among the accessible energy states under the wavelengths used, which gives rise to absorptive nonlinearities (changes in absorption) as well as refractive nonlinearities (changes in the refractive index). In this context, we studied<sup>40</sup> the ultrafast dynamics and third-order nonlinear optical properties of TOPs **23a**, **i** and **b** using a single beam Z-scan technique with femtosecond (fs) and nanosecond (ns) pulses at respective near-IR and visible wavelengths. Porphyrins **23a**, **b** and **i** possess unique third-order nonlinear optical behaviour with a wide spectral range and show both ESA and TPA in the same solvent, but at different

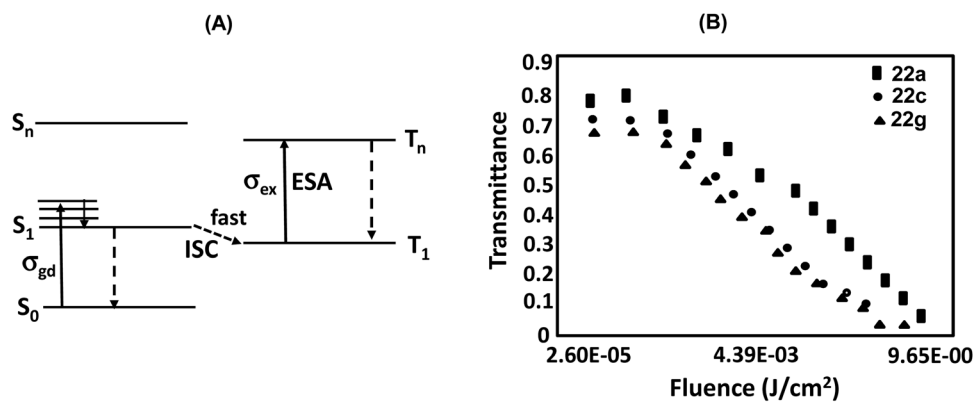


Fig. 17 (A) Proposed energy-level model depicting photophysical processes (ISC: intersystem crossing, ESA: excited state absorption leading to RSA); (B) normalized transmittance of **22a**, **22c** and **22g** as a function of the fluence of laser pulse (527 nm). Reproduced with permission from ref. 39. Copyright 2016, The Royal Society of Chemistry.

Table 2 Photophysical properties, singlet excited-state lifetimes, decay profiles and optical limiting values of **22a**, **22c** and **22g**.<sup>39</sup>

	$\sigma_{\text{ex}}^a$ ( $\text{cm}^2$ )	$\sigma_{\text{g}}^b$ ( $\text{cm}^2$ )	$\sigma_{\text{ex}}/\sigma_{\text{g}}^c$	$\epsilon_{\text{H}}^d$ (eV)	$\epsilon_{\text{L}}^d$ (eV)	$\epsilon_{\text{H}} - \epsilon_{\text{L}}^d$ (eV)	$\eta^e$	$\tau_s^f$ (ps)	$K^g$ ( $\text{s}^{-1}$ )	Fluence threshold ( $\text{J cm}^{-2}$ )
<b>22a</b>	$8.32 \times 10^{-17}$	$3.32 \times 10^{-19}$	250	-4.86	-2.54	-2.32	1.16	170	$5.9 \times 10^9$	0.310
<b>22c</b>	$1.50 \times 10^{-16}$	$3.01 \times 10^{-19}$	498	-4.89	-2.78	-2.11	1.05	1500	$6.6 \times 10^8$	0.531
<b>22g</b>	$6.27 \times 10^{-17}$	$3.18 \times 10^{-19}$	197	-4.86	-2.55	-2.31	1.15	140	$7.1 \times 10^9$	0.217

<sup>a</sup> Excited-state cross-section. <sup>b</sup> Ground-state cross-section. <sup>c</sup> Ratio of excited to ground-state absorption cross-section. <sup>d</sup> Energy of HOMO and LUMO levels. <sup>e</sup> Derived from Koopman's theorem:  $\eta = (\epsilon_{\text{H}} - \epsilon_{\text{L}})/2$ . <sup>f</sup> Singlet excited-state lifetime. <sup>g</sup> Decay constant.



**Table 3** Energies of the HOMO (H) and LUMO (L) orbitals, excited state and ground state absorption cross-sections, TPA cross-sections, average polarizability, nonlinear absorption and refractive coefficients of **23a**, **i** and **b**<sup>40</sup>

	$\varepsilon_H/\varepsilon_L^a$ (eV)	$\sigma_{ex} \times 10^{-21b}$ (m <sup>2</sup> )	$\sigma_g \times 10^{-23}$ (m <sup>2</sup> ) <sup>b</sup>	$\frac{\sigma_{ex}}{\sigma_g^b}$	$\sigma^{(2)c}$ (GM)	$\alpha \times 10^{-41d}$ (cm <sup>2</sup> V <sup>-1</sup> )	$\beta \times 10^{-8e}$ (m W <sup>-1</sup> )	$\gamma \times 10^{-15f}$ (m <sup>2</sup> W <sup>-1</sup> )	$\tau_s^g$ (ps)	$K^h$ (s <sup>-1</sup> )
<b>23a</b>	-4.49/-2.43	24.9	3.43	725	19.4 (±0.3)	1121.49	2.77 (4.66 × 10 <sup>-10</sup> )	-5.91 (-4.78)	417	1.63 × 10 <sup>9</sup>
<b>23i</b>	-4.53/-2.52	7.49	9.96	75	29.0 (±0.4)	1141.10	2.90 (7.01 × 10 <sup>-10</sup> )	-1.29 (-7.92)	513	1.50 × 10 <sup>8</sup>
<b>23b</b>	-4.43/-2.38	7.60	6.64	114	13.0 (±0.3)	1096.48	2.18 (3.97 × 10 <sup>-10</sup> )	-5.27 (-5.57)	336	1.52 × 10 <sup>9</sup>

<sup>a</sup> H-L energies (TD-DFT). <sup>b</sup> Excited-state and ground-state absorption cross-section values at 527 nm and the ratio of excited to ground-state absorption cross-section. <sup>c</sup> TPA cross-section values at 800 nm in SI units, where 1 GM = 10<sup>-50</sup> cm<sup>4</sup> s photon<sup>-1</sup>. <sup>d</sup> Average polarizability (Gaussian 09). <sup>e</sup> Calculated in DCM at 527 nm; the values in parenthesis were determined at 800 nm. <sup>f</sup> Calculated in DCM at 527 nm; the values in parenthesis were determined at 800 nm. <sup>g</sup> Singlet excited-state lifetime. <sup>h</sup> Decay constant.

wavelengths and pulse widths. While ESA mediated RSA was observed at 527 nm, two-photon absorption (TPA) was observed at 800 nm. The high nonlinear refractive index coefficient and nonlinear absorption coefficient values and the fast response times were attributed to the polarizable  $\pi$ -electrons of the cyclic conjugated aromatic porphyrin framework. Our proposed mechanism of third-order nonlinearity was verified using

ultrafast transient absorption spectroscopy. The TPA cross-section values (at 800 nm, Z-scan) with 50 fs laser pulses were in the range of 10 to 30 GM and are given in Table 3. Furthermore, since the  $\pi$ -conjugation pathway of **23a**, **i** and **b** is identical, the H-L energies (Table 3) as well as the H-L gaps were small and of the same order in parallel with the TOPs **23a**, **i** and **b**. The values of the TPA cross-sections (Table 3) are in

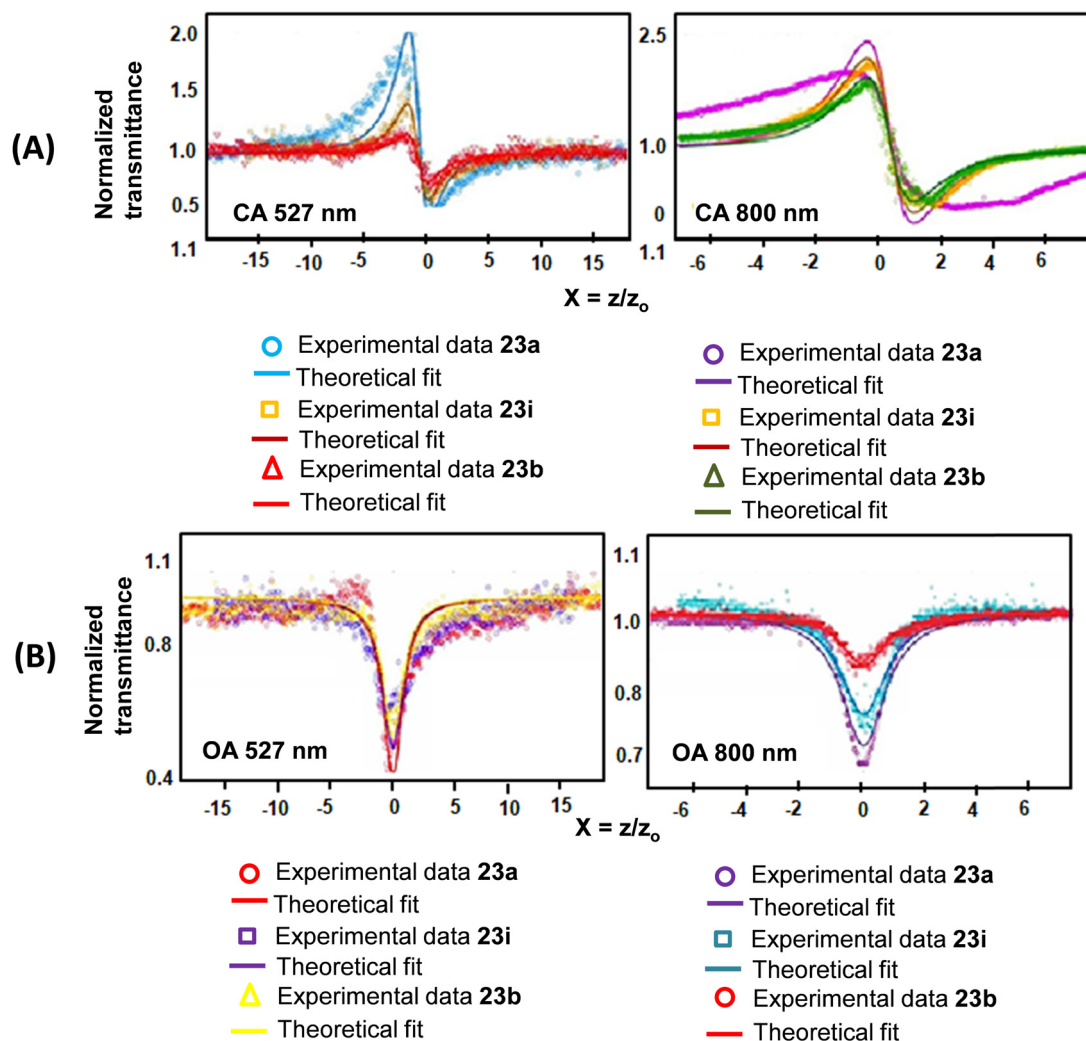


**Fig. 18** Z-scan traces of **23a**, **23i** and **23b** in DCM under (A) closed aperture (CA) and (B) open aperture (OA) conditions at (i) 527 nm and at (ii) 800 nm. Reproduced with permission from ref. 40. Copyright 2016, The Royal Society of Chemistry.



agreement with the calculated molecular polarizability (converse of molecular hardness,  $Z$ ). Among the three compounds studied the presence of  $p$ -BrC<sub>6</sub>H<sub>4</sub> substituents at *meso*-positions in **23i** seems to render more polarizability leading to the largest TPA cross-section value (Table 3). The reduction in transmittance (Fig. 18) for these porphyrins as measured by the open aperture (OA) Z-scan technique was independent of nonlinear refraction and used to determine  $\beta$  (Table 3). The OA traces further inferred that absorption was intensity dependent and the maximum absorption occurred at the focal point of the lens, where the on-axis intensity of the beam is maximum. In order to account for the mechanism of nonlinear absorption, occurring in **23a**, **b** and **i**, the cross sections of the ground and excited states were calculated.

The excited to ground state absorption cross-section ratio ( $\sigma_{\text{ex}}/\sigma_{\text{gd}}$ ) (Table 3) was the maximum for **23a** having an unsubstituted phenyl ring at the *meso* position of the porphyrin, while **23b** bearing a  $p$ -BrC<sub>6</sub>H<sub>4</sub> group at the *meso* position recorded the minimum value. The population of the excited states after  $ns$  (100 ns) pulse excitations in the case of **23a** was nearly 750 times greater (due to faster ISC) in the excited state compared to the ground state. This indicated the initial build-up of population at the singlet excited state, which is transferred to the triplet states and is responsible for ESA leading to RSA. Furthermore, RSA is not due to TPA because if the nonlinear absorption was due to TPA then  $\beta$  should have remained constant by varying (increasing) the axis fluence. However, we observed a decrease in  $\beta$  with increasing axis fluence.<sup>40</sup> The nonlinear absorption coefficients  $\beta$  determined through both OA and close aperture (CA) techniques at 527 nm and 800 nm for **23a**, **b** and **i** were identical. While the positive values of  $\beta$  indicated RSA, the negative value of nonlinear refractivity ( $\gamma$ ) was attributed to the self-defocusing effect.

## 4. Concluding remarks

The exciting photophysical properties, charge transport and nonlinear optical behaviour of organic semiconductors such as tetrathia/tetraoxa[22]porphyrin(2.1.2.1)s await further exploration. This is clearly indicated by the development of chemistry and applications of these *meso*-substituted porphyrinoids by us in the past decade. Refinement in the synthetic approaches is much desired to improve the yield of these porphyrinoids as well as to incorporate aliphatic substituents at the 5- and 16-positions of these porphyrinoids. This has constituted a severe limitation of the work reported by us as we could not oxidize the 5-, 15-dihydro counterparts to obtain the corresponding fully aromatized porphyrinoids. Electrochemical switching of these systems between  $22\pi$  aromatic and  $20\pi$  antiaromatic states is another interesting attribute and isolation of stabilized salts of the dicationic antiaromatic species would be interesting. Simultaneously, placing suitable substituents at the macrocyclic rim would provide immense opportunities for obtaining donor-acceptor type porphyrins for applications related to semiconducting

charge transport and other optoelectronic applications such as redox switchable nonlinear optical materials. Additionally, the rich collection of porphyrinoids discussed in this personal account will provide an opportunity to understand the interplay between aromaticity and structure. On a more fundamental level, various porphyrin analogues presented in this article serve to highlight what is still relatively “unexplored territory” in porphyrin chemistry. We thus predict that the area of *meso*-substituted porphyrins will constitute an area of considerable growth in the years to come offering immense opportunities in the area of synthesis, physicochemical analysis, metal complexation chemistry, anion recognition, catalysis, redox switching and organic electronics.

## Conflicts of interest

There are no conflicts to declare.

## Acknowledgements

K. S. thanks SERB (DST, New Delhi) for the grant EMR/2017/000520 and Guru Nanak Dev University, Amritsar for facilities. We express our sincere gratitude to the colleagues with whom we have been collaborating over the years on the device fabrication etc. as well as to our skilled students.

## References

- (a) *The Porphyrin Handbook*, ed. K. Kadish, K. M. Smith and R. Guilard, Academic Press, London, 2000, vol. 1–20; (b) S. Hiroto, Y. Miyaki and H. Shinokubo, *Chem. Rev.*, 2017, **117**, 2910; (c) S. Saito and A. Osuka, *Angew. Chem., Int. Ed.*, 2011, **50**, 44342; (d) *Handbook of Porphyrin Science*, ed. K. Kadish, K. M. Smith and R. Guilard, World Scientific, London, 2010; (e) T. K. Chandrashekar and S. Venkataraman, *Acc. Chem. Res.*, 2003, **36**, 676; (f) R. Misra and T. K. Chandrashekar, *Acc. Chem. Res.*, 2008, **41**, 265; (g) M. O. Senge, N. N. Sergeeva and K. J. Hale, *Chem. Soc. Rev.*, 2021, **50**, 4730; (h) B. Sekaran and R. Misra, *Coord. Chem. Rev.*, 2022, **453**, 214312.
- (a) M. O. Senge, M. Fazekas, E. G. A. Notaras, W. J. Blau, M. Zawadzka, O. B. Locos and E. M. NiMhuirheartaigh, *Adv. Mater.*, 2007, **19**, 2737; (b) A. Chaudhary, A. Srinivasan and T. K. Chandrashekar, in *Handbook of Porphyrin Science*, ed. K. Kadish, K. M. Smith and R. Guilard, World Scientific, London, 2014, p. 271; (c) M. Janghour and M. Adineh, *J. Photochem. Photobiol., A*, 2017, **341**, 31; (d) J. V. Krishna, P. Mrinalini, S. Prasanthkumar and L. Giribabu, *Dye-Sensitized Solar Cells*, Academic Press, New York, NY, USA, 2019, ch. 7, pp. 231–284; (e) J. Kesters, P. Verstappen, M. Kelchtermans, L. Lutsen, D. Vanderzande and W. Maes, *Adv. Energy Mater.*, 2015, **5**, 1500218; (f) A. Tebo, C. Herrero and A. Aukauloo, in *Handbook of Porphyrin Science*, ed. K. Kadish, K. M. Smith and R. Guilard, World Scientific, London, 2014, p. 196; (g) T. W. Liu, E. Huynh,





- D. Goswami, *J. Am. Chem. Soc.*, 2005, **127**, 11608; (g) C. Wang, G. Shi, Z. Zhu, S. Luo, W. Sun, W. Jiao, R. Gao, G. Fan and Y. Song, *Opt. Mater.*, 2020, **100**, 109621; (h) S. M. LeCours, H.-W. Guan, S. G. DiMagno, C. H. Wang and M. J. Therien, *J. Am. Chem. Soc.*, 1996, **118**, 1497.
- 38 P. Kaur and K. Singh, *Chem. Rec.*, 2022, e202200024.
- 39 K. Singh, S. Arora, K. Makhal, P. Kaur and D. Goswami, *RSC Adv.*, 2016, **6**, 22659.
- 40 K. Makhal, P. Kaur, S. Arora, D. Goswami and K. Singh, *J. Mater. Chem. C*, 2016, **4**, 9445.

